

## **Wall Climbing Micro Ground Vehicle (MGV)**

**by Ian Bryant, Howard Carpenter, Asha Hall, and Mark Bundy**

**ARL-TR-6628**

**September 2013**

## **NOTICES**

### **Disclaimers**

The findings in this report are not to be construed as an official Department of the Army position unless so designated by other authorized documents.

Citation of manufacturer's or trade names does not constitute an official endorsement or approval of the use thereof.

Destroy this report when it is no longer needed. Do not return it to the originator.

# **Army Research Laboratory**

Aberdeen Proving Ground, MD 21005

---

---

**ARL-TR-6628**

**September 2013**

---

## **Wall Climbing Micro Ground Vehicle (MGV)**

**Ian Bryant, Howard Carpenter, Asha Hall, and Mark Bundy**  
**Vehicle Technology Directorate, ARL**

REPORT DOCUMENTATION PAGE				Form Approved OMB No. 0704-0188	
<p>Public reporting burden for this collection of information is estimated to average 1 hour per response, including the time for reviewing instructions, searching existing data sources, gathering and maintaining the data needed, and completing and reviewing the collection information. Send comments regarding this burden estimate or any other aspect of this collection of information, including suggestions for reducing the burden, to Department of Defense, Washington Headquarters Services, Directorate for Information Operations and Reports (0704-0188), 1215 Jefferson Davis Highway, Suite 1204, Arlington, VA 22202-4302. Respondents should be aware that notwithstanding any other provision of law, no person shall be subject to any penalty for failing to comply with a collection of information if it does not display a currently valid OMB control number.</p> <p><b>PLEASE DO NOT RETURN YOUR FORM TO THE ABOVE ADDRESS.</b></p>					
1. REPORT DATE (DD-MM-YYYY) September 2013		2. REPORT TYPE Final		3. DATES COVERED (From - To) June 2012	
4. TITLE AND SUBTITLE Wall Climbing Micro Ground Vehicle (MGV)				5a. CONTRACT NUMBER	
				5b. GRANT NUMBER	
				5c. PROGRAM ELEMENT NUMBER	
6. AUTHOR(S) Ian Bryant, Howard Carpenter, Asha Hall, and Mark Bundy				5d. PROJECT NUMBER	
				5e. TASK NUMBER	
				5f. WORK UNIT NUMBER	
7. PERFORMING ORGANIZATION NAME(S) AND ADDRESS(ES) U.S. Army Research Laboratory ATTN: RDRL-VTM Aberdeen Proving Ground, MD 21005				8. PERFORMING ORGANIZATION REPORT NUMBER ARL-TR-6628	
9. SPONSORING/MONITORING AGENCY NAME(S) AND ADDRESS(ES)				10. SPONSOR/MONITOR'S ACRONYM(S)	
				11. SPONSOR/MONITOR'S REPORT NUMBER(S)	
12. DISTRIBUTION/AVAILABILITY STATEMENT Approved for public release; distribution unlimited.					
13. SUPPLEMENTARY NOTES asha.j.hall.civ@mail.mil					
14. ABSTRACT The increasing desire to remove Soldiers from high-risk situations such as reconnaissance and maintenance of buildings and infrastructure has spawned the idea of wall-climbing robots. Such robots use techniques ranging from magnets to bio-mimicry in order to climb vertical and inverted surfaces. The focus of this project is to run a comparison analysis of different vortex adhesion base plates, which would result in an improvement on the fundamental design of a robotic wall climber. This study includes initial experimentation of inverted wing inspired base plates created to increase the adhesion forces on the robot. The results show that a flat plate with a full shroud can generate low pressures between the wall and itself while holding roughly 7 times its own weight, ~1.93 kg. Our research has indicated that the inverted wing base plates create additional downward forces that are absent in the base plate. Lastly, by channeling airflow from the inlets to the impeller, the turbulent airflow that disrupts the vortex has been eliminated, thus improving performance.					
15. SUBJECT TERMS Wall climbing robot, micro ground vehicle, impeller design					
16. SECURITY CLASSIFICATION OF:			17. LIMITATION OF ABSTRACT UU	18. NUMBER OF PAGES 36	19a. NAME OF RESPONSIBLE PERSON Asha J. Hall
a. REPORT Unclassified	b. ABSTRACT Unclassified	c. THIS PAGE Unclassified			19b. TELEPHONE NUMBER (Include area code) (410) 278-8036

---

## Contents

---

<b>List of Figures</b>	<b>iv</b>
<b>List of Tables</b>	<b>v</b>
<b>1. Introduction/Background</b>	<b>1</b>
<b>2. Design Methodology</b>	<b>2</b>
<b>3. Airfoil Design</b>	<b>3</b>
<b>4. Experimentation</b>	<b>5</b>
<b>5. Results and Discussion</b>	<b>7</b>
5.1 Flow Visualization .....	7
5.2 Effects Of Pressure On The Type Of Control Plate .....	9
<b>6. Summary and Conclusion</b>	<b>15</b>
<b>7. References</b>	<b>17</b>
<b>Appendix A. Vortex Theory</b>	<b>19</b>
<b>Appendix B. Tables</b>	<b>21</b>
<b>Appendix C. Conversion Calculations</b>	<b>25</b>
<b>Distribution List</b>	<b>26</b>

---

## List of Figures

---

Figure 1. Inverted wing shape in a velocity flow simulation.....	2
Figure 2a–c. Blade orientations from left to right, forward inclined, radial, and backward inclined. 3	3
Figure 3a–f. The 6 impeller designs with different blade shapes and numbers.....	3
Figure 4. (a) Circular airfoil plate with vanes, (b) rectangular airfoil plate with vanes, (c) circular airfoil plate, no vanes, and (d) rectangular airfoil plate, no vanes. ....	4
Figure 5. Redirection cone assembly. ....	5
Figure 6. ARL Active perching device. ....	5
Figure 7. (a) Test stand setup and (b) test platform stage with holes for the pitot tube inserts. ....	6
Figure 8. Pressure sensor. ....	6
Figure 9. Flow visualization setup. ....	7
Figure 10a–c. Flow visualization results. ....	8
Figure 11. Pressure results for the flat and curved blade impellers respectively. Units are in kPa. ....	9
Figure 12. Effect of voltage on the carrying and dragging capacity for the flat plate control subject at full shroud. The weight of the robot is included in the normal force. ....	10
Figure 13. Control plate on an inverted surface.....	10
Figure 14. Control plate on a brick wall. ....	10
Figure 15. Effects of ride height on pressure for a rectangular vaned plate of varying shroud coverage. ....	11
Figure 16. Effects of ride height on pressure for a rectangular unvaned plate of varying shroud coverage. ....	11
Figure 17. Effects of ride height on pressure for a circular vaned plate of varying shroud coverage. ....	12
Figure 18. Effects of ride height on pressure for a circular unvaned plate of varying shroud coverage. ....	12
Figure 19. Comparison of all experimental plates with full shroud coverage. ....	12
Figure 20. Pressure field test of control plate. ....	13
Figure 21. Pressure field test of rectangular vaned plate. ....	14
Figure 22. Rectangular vaned plate with internal channels. ....	14
Figure 23. Pressure field test of channeled plate design. ....	15
Figure 24. Rectangular vaned plate with channels on an inverted surface. ....	15

---

## List of Tables

---

Table B-1. Table of information used to generate figure 10. Units are in mm and kPa. ....	21
Table B-2. Table of information used to generate figure 11. Units are in mm and kPa. ....	21
Table B-3. Table of information used to generate figure 12. Units are in mm and kPa. ....	22
Table B-4. Table of information used to generate figure 13. Units are in mm and kPa. ....	22
Table B-5. Table of information used to generate figure 14. Units are in mm and kPa. ....	23
Table B-6. Table of information used to generate figure 9.....	23

INTENTIONALLY LEFT BLANK.



---

## 1. Introduction/Background

---

Within the last 10 years, great interest has arisen for the development of wall-climbing robots. Inspiration for this development came from the need of taking the Warfighter out of potentially dangerous situations. Wall-climbing micro vehicles offer the ability to provide situational awareness to the Warfighter furnishing the Soldier with the capability to make fast accurate decisions. In today's battlefield, the Warfighter must retrieve a wide variety of information including tactical intelligence, terrestrial weather effects, squad command locations, and space environmental reports along with finding the enemy. In order to achieve such operational superiority, combat commanders depend on platforms that can provide functional intelligence to support their mission. Some robots, such as TALON and Telemax, have already been developed for high risk missions such as explosive ordinance disposal and fire rescue. Other uses for these robots are cleaning and maintenance, inspection of aircraft and buildings, and surveillance operations (Sadegh and Xiao, 2007). However, these robots did not have the ability to navigate very steep or vertical surfaces, so they are limited to the areas of relatively flat surfaces and mild inclines.

Several techniques have been used to develop wall-climbing robots. The four primary techniques are (1) magnetic attraction, (2) vacuum suction, (3) bio-mimetic techniques such as gecko pads, and (4) adhesion forces generated by aerodynamic principles, also known as vortex adhesion (Sadegh and Xiao, 2007). Each technique has its advantages and disadvantages. For example, magnets are capable of generating large attractive forces, but are limited to ferrous surfaces. Vacuum suction, such as in suction cups, also has the ability to create large adhesion forces, but will only work on flat and smooth surfaces. Gecko pads have the ability to climb almost any surface given that the surface is perfectly clean. Vortex adhesion does not require a perfect seal like vacuum suction and has the ability to travel over porous surfaces such as brick and concrete. The issue with this technique, however, is that when larger voids are encountered, the skirting technique is compromised.

In this study, we explore the vortex method along with Bernoulli's Principle as the primary means of adhesion. Bernoulli's effect (assuming incompressible air flow) states that there is an increase in the speed of the fluid simultaneously with the decrease in pressure. In the case of the inverted airfoil design, the cord length is longer on the bottom of the airfoil, thereby the air molecules are traveling at greater speeds underneath, creating a lower pressure (figure 1). This mechanism creates a net downward force. In an attempt to increase the efficiency of airflow under the robot, different styles of base plates are used. Typically, flat bases with skirting are used in this kind of robot, but these plates do not optimize the airflow. In this experiment, a known flat plate technology is used as the baseline while plates with an inverted airfoil shape are

tested for improved performance. It is believed that the inverted wing shape will allow for smoother airflow and will create a lower pressure vortex between the wall and the robot. In theory, a lower pressure will generate a larger adhesion force to the wall. In addition, it is believed that these plates will enable the ability to navigate steep or even vertical surfaces.

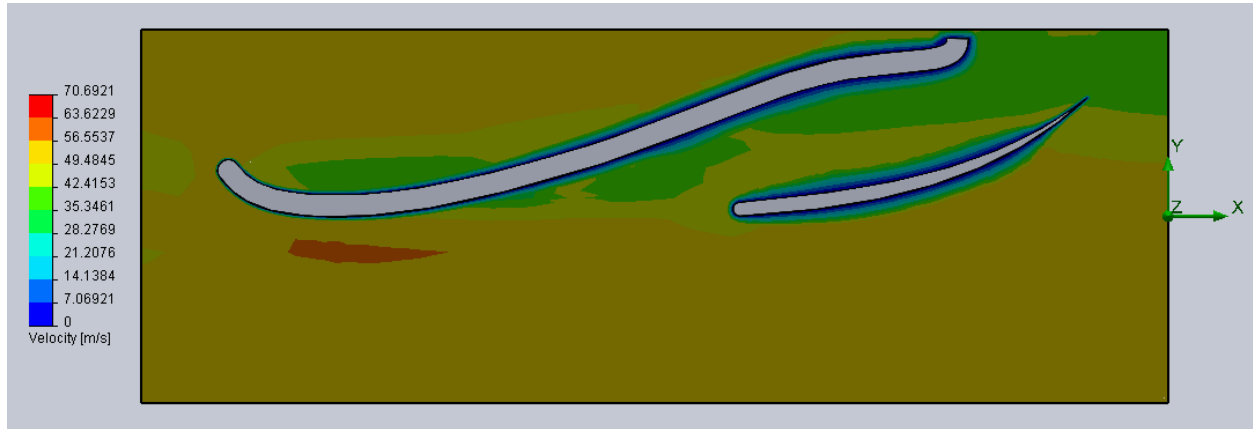


Figure 1. Inverted wing shape in a velocity flow simulation.

---

## 2. Design Methodology

---

The central component of this robot is the vortex generated to create a low pressure system between the robot base and the wall or ceiling. When designing an impeller one may choose from an axial or centrifugal impeller. Impellers are designed so that they are used for a specific application. If used for other purposes, severe mechanical damage may be inflicted upon the impeller. In this situation, a centrifugal impeller is chosen due to its ability to generate the lowest pressures. While axial impellers are capable of moving large volumes of air, they tend to cavitate in these situations which could damage the impeller. Generally, a centrifugal impeller has 3 different blade orientations to choose from. These designs are displayed in figure 2. For this study, a centrifugal impeller is placed over a central inlet hole to pull air from under the robot and generate a vortex (please refer to appendix A on vortex theory).

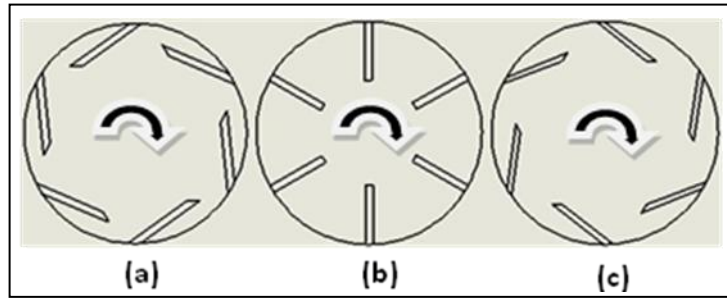


Figure 2a–c. Blade orientations from left to right, forward inclined, radial, and backward inclined.

Both the forward and backward inclined blades are capable of generating the low pressures needed for adhesion. However, the backward inclined blades allow for the impeller to rotate at higher speeds which creates additional low pressures. Radial blades are not considered because they lack the ability to generate low pressures. For these reasons, the use of backward inclined blades were employed during the experimentation phase.

Lastly, the shape and number of the blades were altered. It is unknown what number of blades is needed to allow for maximum airflow while still maintaining a low pressure. Using these variables and the parameters listed above, 6 impellers are designed and shown in figure 3.

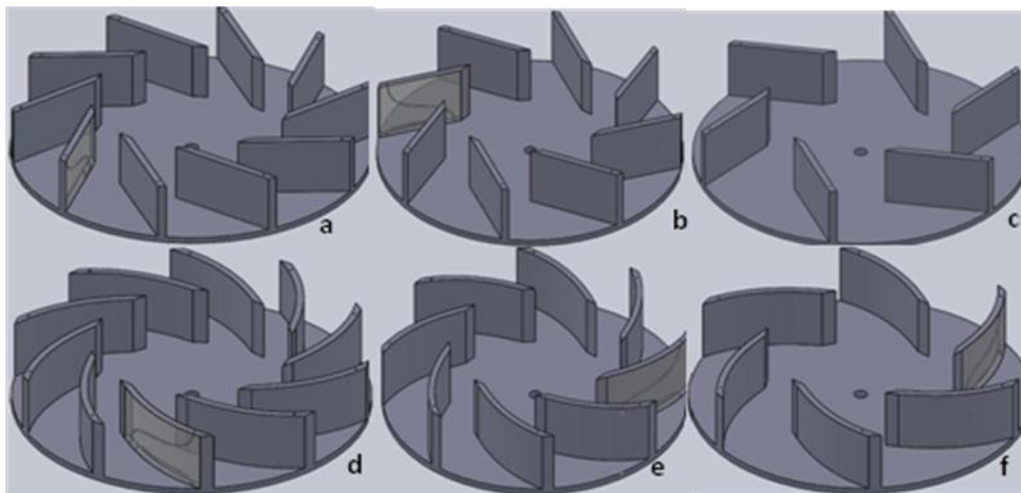


Figure 3a–f. The 6 impeller designs with different blade shapes and numbers.

---

### 3. Airfoil Design

---

As for the airfoil design, typical vortex-generating robots have a means of containing the vortex underneath the robot. To do this, a 68-gauge polyester sheet is placed around the edges of the

base plates to help contain the vortex. This material is chosen because it will conform to the minor contours apparent in some surfaces.

A new design concept to be tested uses inverted wing designs to create downward forces on the robot. This method uses the same principles that a wing uses to generate lift. As air passes under the base plate, its velocity increases, which decreases the pressure under the base plate. On the top side of the base plate, the air is decelerating, which increases pressure on the top side. This difference in pressure creates forces that act toward the surface the robot is sitting on, which will aid in adhesion. This concept is similar to the one used in Formula 1 racing cars to create more downward forces on the car while it is driving. Lift forces are quite large on Formula One racing cars and in order to mitigate the lift forces, the shape of the car is modeled after an inverted wing to create downward forces that will press the race car against the surface of the track to create an aerodynamic grip. For preliminary experimentation, an inverted airfoil shape similar to that of a NACA 8303 is applied to both rectangular and circular base shapes. Internal vanes similar to a NACA 8504 are also included in the design, as seen in figures 4a and b. Figures 4c and d show the same plates without internal vanes. The primary wing has a theoretical lift coefficient of 2.23 while the vanes have a theoretical lift coefficient of 2.42. These coefficients are found at  $9.27^\circ$  and  $18.6^\circ$  angles of attack. Theoretically, these plates should create downward forces acting on the robot which could possibly eliminate or reduce the necessity of a shroud.

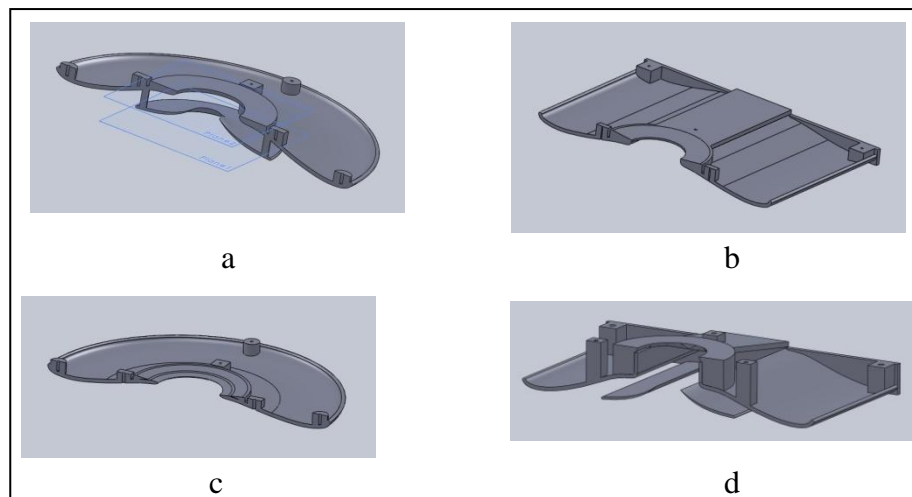


Figure 4. (a) Circular airfoil plate with vanes, (b) rectangular airfoil plate with vanes, (c) circular airfoil plate, no vanes, and (d) rectangular airfoil plate, no vanes.

To create an additional force on the robot, a thrusting cone (figure 5) is incorporated into the preliminary design of the control platform. This concept is used on the City Climber robot from the City College of New York to redirect exhaust air from the impeller back in an axial direction (Sadegh and Xiao, 2007). The redirected air should create a downward force on the robot, helping it adhere to the wall.

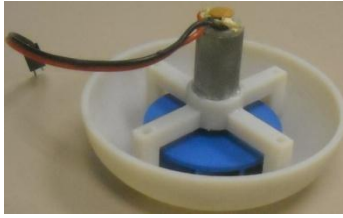


Figure 5. Redirection cone assembly.

For a perching device, a simple “L” shaped hook is mounted to the robot so it may hang onto ledges. Figure 6 shows the perching hook holding the control plate to a ledge while the impeller is off.



Figure 6. ARL Active perching device.

The drive system consists of two wheels placed at the center of the plate. This setup allows for easy mobility and quick turning through the use of differential steering. Both perching and drive systems are controlled by a handheld Spektrum transmitter.

---

## 4. Experimentation

---

In this experiment, the robot is designed to be roughly 15 cm x 15 cm. A robot of this size should be able to navigate over moderate gaps commonly found on buildings and infrastructure. The experimental plates, impeller, and motor mount for the robot are prototyped on an Objet 260v 3D printer using a VeroGray material. Later, both the impeller and the motor mount are printed on a Fortus 400mc 3D printer using ABS plastic. The impeller is later printed out of a more durable ULTEM (polyetherimide) plastic. The control plate is cut from a thin acrylic sheet by a Universal VersaLaser.

To assess the performances of the experimental bases, each plate is placed on top of a testing platform as seen in figure 7. The platform uses a 5-in D-4V low pressure sensor (figure 8) in conjunction with a power source and voltmeter to take pressure readings. When 4 V is supplied

to the sensor, it can read up to  $\pm 5$  in of  $H_2O$  of pressure change. In this experiment, measurements are taken with increasing shroud coverage at ride heights ranging from 0 to 3.6 mm at 0.4-mm intervals. To convert voltages into pressure, refer to the conversion equation in appendix C. A Berkley 23-kg electronic scale is then used to verify the data obtained from the sensor. This same scale is then used to collect data on the driving force of the robot. The driving force test is conducted on both a horizontal and vertical surface.

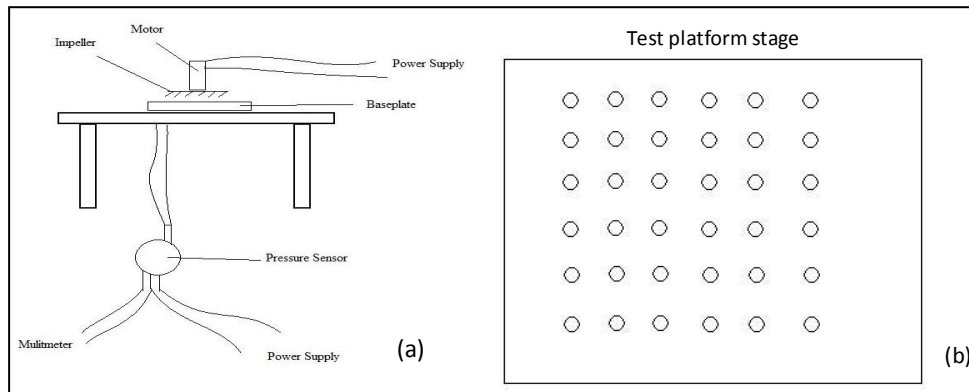


Figure 7. (a) Test stand setup and (b) test platform stage with holes for the pitot tube inserts.

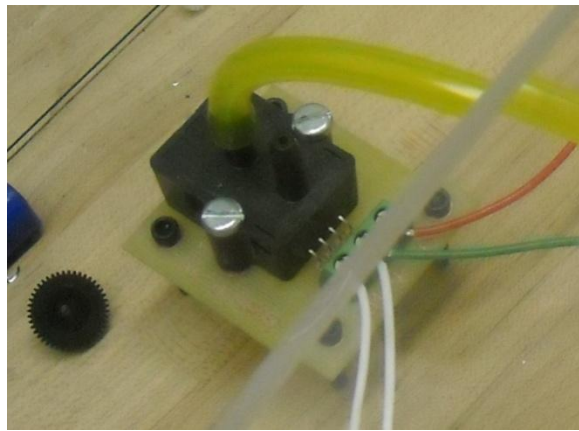


Figure8. Pressure sensor.

The impellers for the flow visualization are printed out of ABS plastic on a Fortus and/or Stratus 3D printer. For assembly on the ground vehicle platform, they are milled out of a lightweight aluminum to withstand the large rotational forces.

The flow visualization is conducted in an 18"x18"x18" water tank with each impeller rotating at 30 RPMs as shown in figure 9. When the impellers are scaled up to 4 times their actual size and are rotating at this frequency, the Reynolds number ( $Re$ ) for the flow matches that for the smaller size. In order to create an accurate representation of the flow through the impeller the

Reynolds numbers must match. To obtain Reynolds number, please refer to equation 1, wherein  $\mu$  is the dynamic viscosity,  $\rho$  is density,  $V$  is voltage, and  $c$  is the Bernoulli constant:

$$Re = \frac{\rho V c}{\mu} \quad (1)$$

Dye is then injected onto the impeller along the axis as it rotates. The dye represents the air particles moving through the impeller.

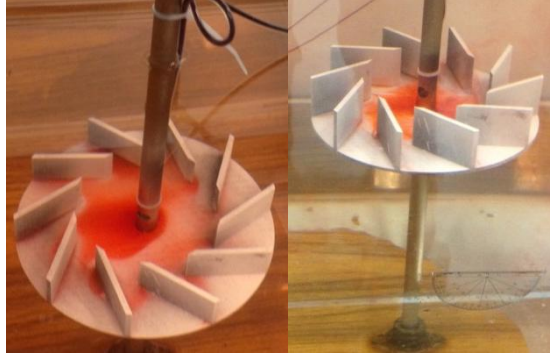


Figure 9. Flow visualization setup.

---

## 5. Results and Discussion

---

### 5.1 Flow Visualization

Figures 10a, b, and c are screen captures of the flow visualization tests for the flat 10 blade, curved 10 blade, and curved 8 blade impellers, respectively.



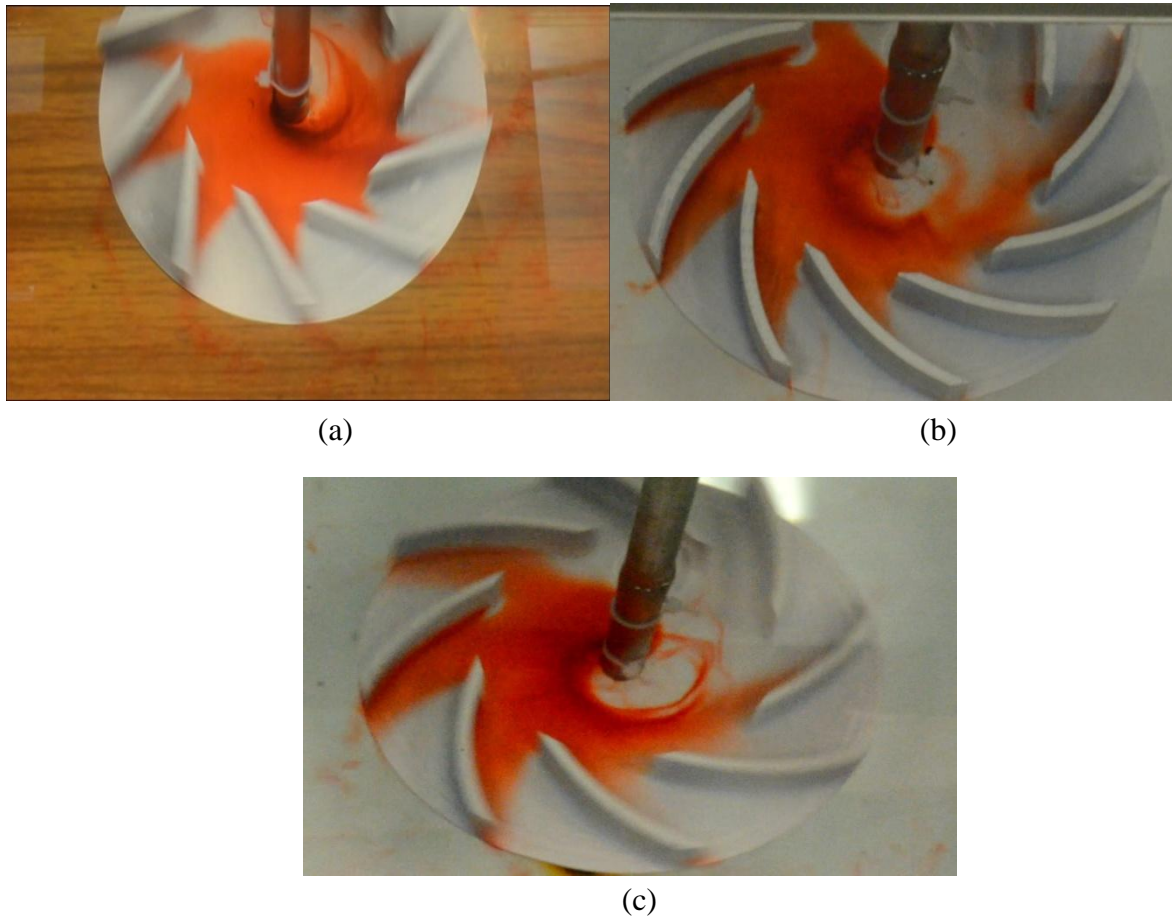


Figure 10a–c. Flow visualization results.

As depicted in figure 10, it is apparent that a vortex is forming at the leading edge of the blades. This is noted by the bubble appearing at the tip of each blade. This vortex could potentially cause the fluid to take more time to flow around each blade which could slow the impeller down. A second similarity between the blades is the presence of vortex shedding. The shedding can be identified by the turbulent dye flow leaving the trailing edge of each blade. The presence of vortex shedding can slow down the rotational velocity and possibly cause damage.

The biggest difference between the different designs is how much of the area between each blade is actually being used by the flow. The flat blade shows that only about 25% of the space is occupied by the dye. This may indicate a restricted flow through the blade which leads to a decrease in performance. Collectively, the curved blade designs showed more flow through the blades by approximately 30–40%.

Figures 11a and b represents the results of the pressure tests for the 10 flat and curved blade impellers, respectively. They appear in the form of a pressure map to represent areas of higher pressure and lower pressure.



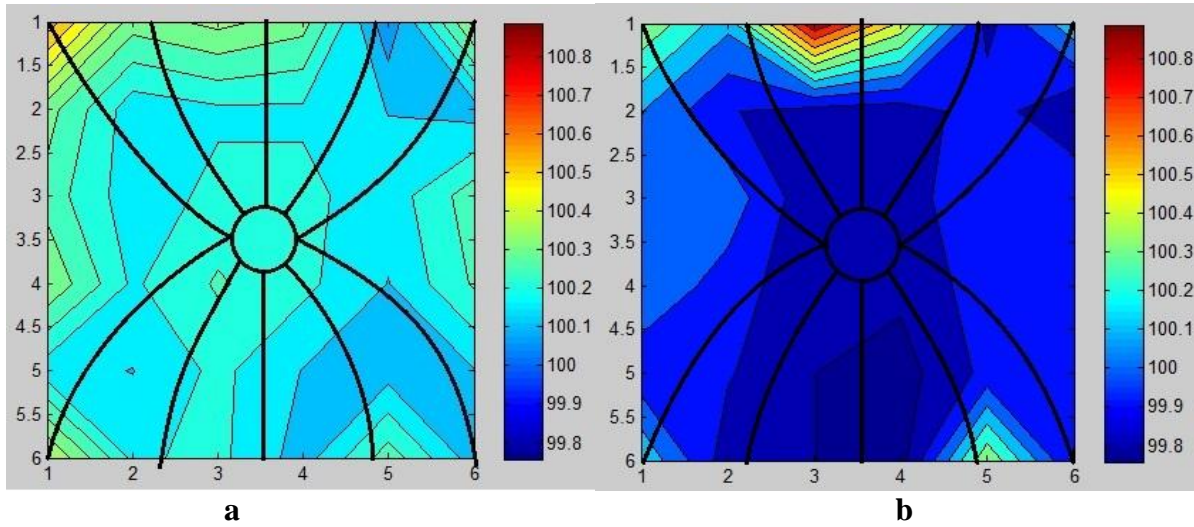


Figure 11. Pressure results for the flat and curved blade impellers respectively. Units are in kPa.

Both figures show regions of lower pressure in the upper left and bottom right corners of the base plate. This unevenness could be caused by an uneven distributed load that comes from the placement of the receiver and the battery. The difference between the two is where the lowest pressures are located and the magnitude of these pressures. For the flat blades, the lowest pressure is roughly 100.1 kPa at a small region in the upper right corner of the plate. The curved blades had a lower pressure of about 99.8 kPa located at the bottom center of the plate. The pressures given here are used to find the adhesive force for each impeller. With flat blades, the vehicle can hold roughly 1.15 kg when with curved blades, it can hold 1.40 kg.

## 5.2 Effects Of Pressure On The Type Of Control Plate

Figure 12 is a graph displaying the results of a force capacity test on the baseline platform. Increasing the voltage input to the motor shows an increase in maximum force load with a maximum force of 1.93 kg. The force just mentioned is the total force of the robot, that is, it is the maximum force allowed before the robot loses contact with its surface. The other two lines represent how much force the robot can pull before the wheels start slipping. This data set is taken on both horizontal and vertical surfaces. As can be seen, the maximum dragging force is roughly 1.22 kg no matter the surface.

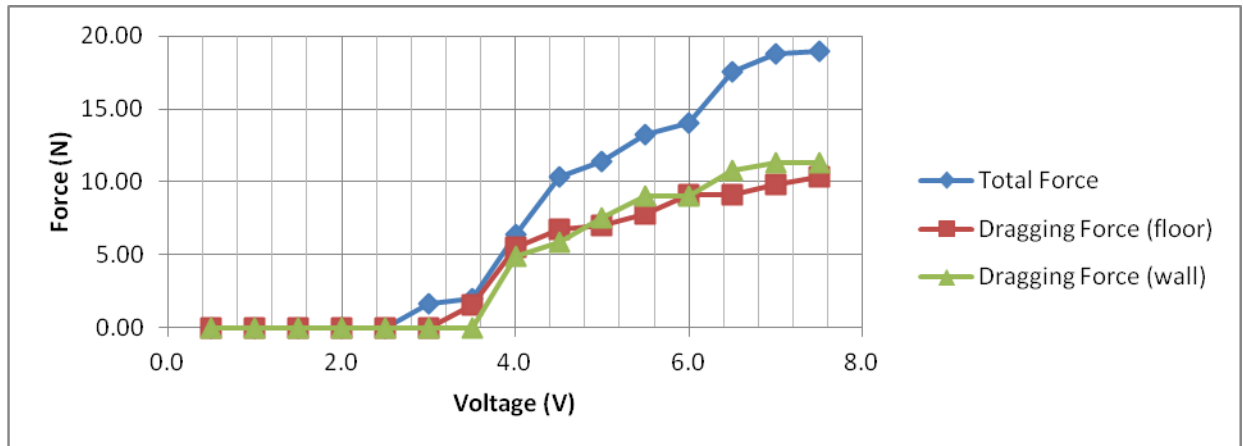


Figure 12. Effect of voltage on the carrying and dragging capacity for the flat plate control subject at full shroud. The weight of the robot is included in the normal force.

Figures 13 and 14 show the control plate during operation on both a brick wall and an inverted surface.

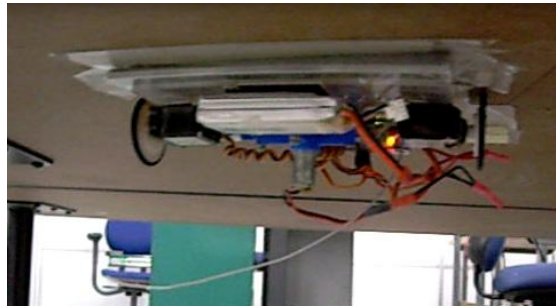


Figure 13. Control plate on an inverted surface.

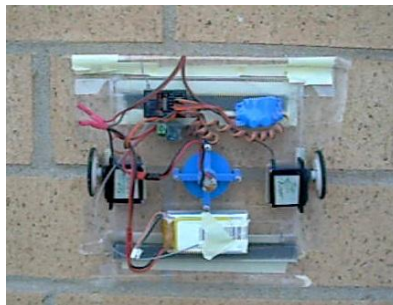


Figure 14. Control plate on a brick wall.

The robot is tested at increasing ride heights to determine the maximum gap size the robot can navigate. That is, if the bottom of the robot is just touching the surface, it will be able to navigate over a gap that is as deep as the maximum ride height. The purpose of the shroud is to help

maintain the low pressures present between the surface and the robot. While a full shroud will be more effective at maintaining the low pressures, it is desired to have less shroud coverage so navigation will be less inhibited. Figures 15–19 describe the effects that shroud coverage and ride height has on pressure (also refer to appendix B for the tables). Analyzing these graphs shows that as shroud coverage decreases, the rate at which pressure equalizes to that of the atmosphere's increases. It can be seen in these figures that every plate has equivalent pressure differentials at zero ride height regardless of the amount of shroud coverage present on the robot. This result may be attributed to the fact that a near perfect seal is formed at zero ride height. However, even a slight change in ride height appears to quickly change these results.

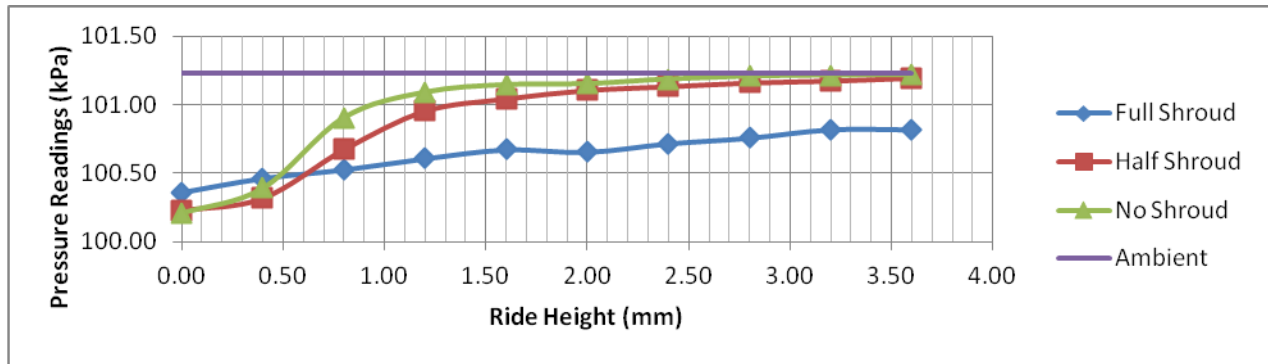


Figure 15. Effects of ride height on pressure for a rectangular vaned plate of varying shroud coverage.

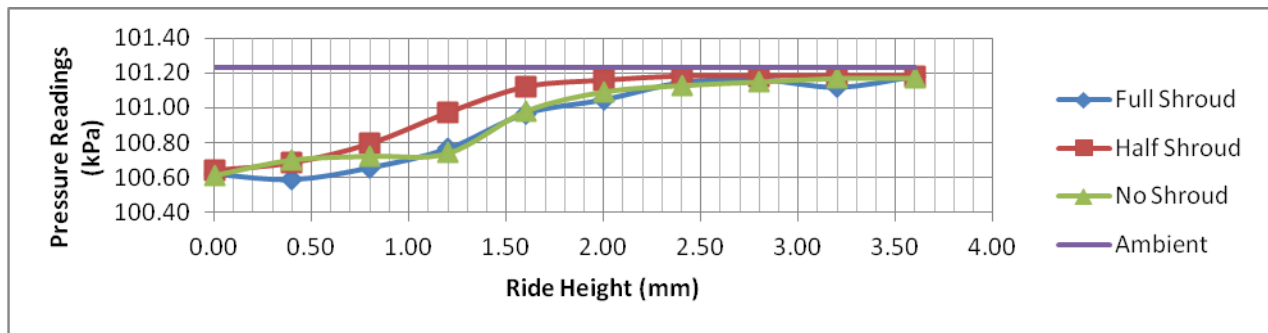


Figure 16. Effects of ride height on pressure for a rectangular unvaned plate of varying shroud coverage.

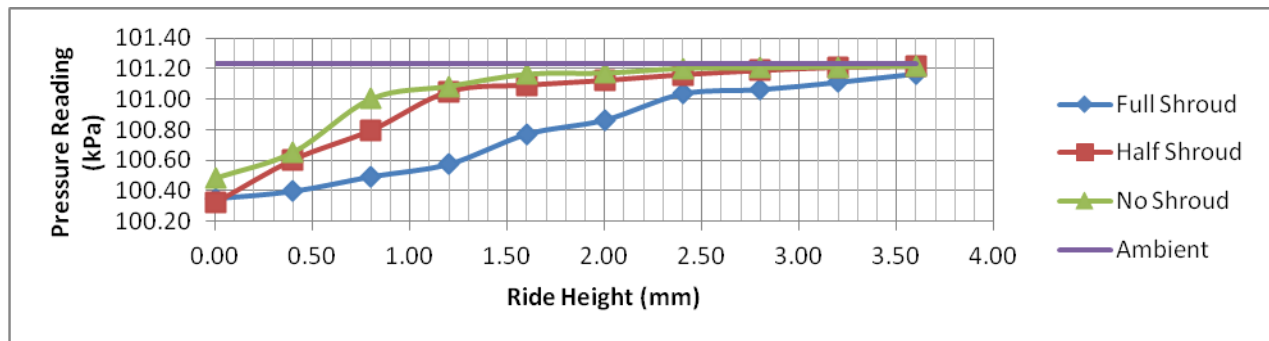


Figure 17. Effects of ride height on pressure for a circular vaned plate of varying shroud coverage.

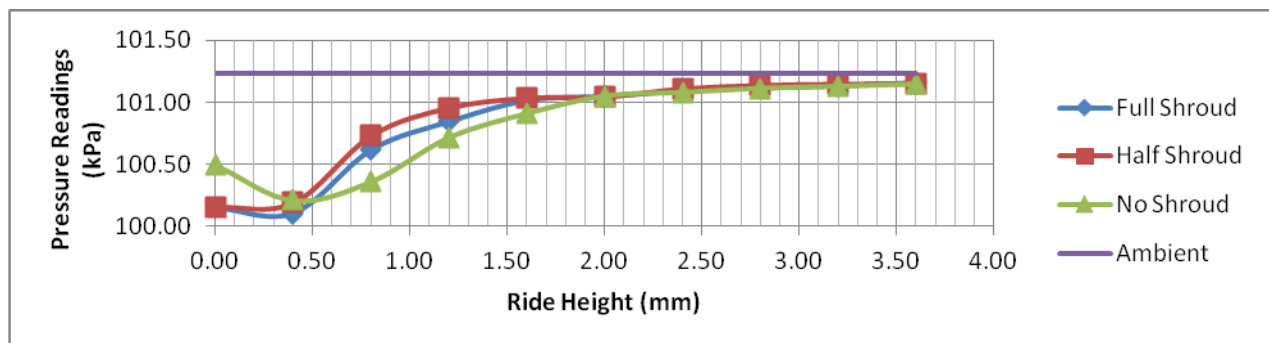


Figure 18. Effects of ride height on pressure for a circular unvaned plate of varying shroud coverage.

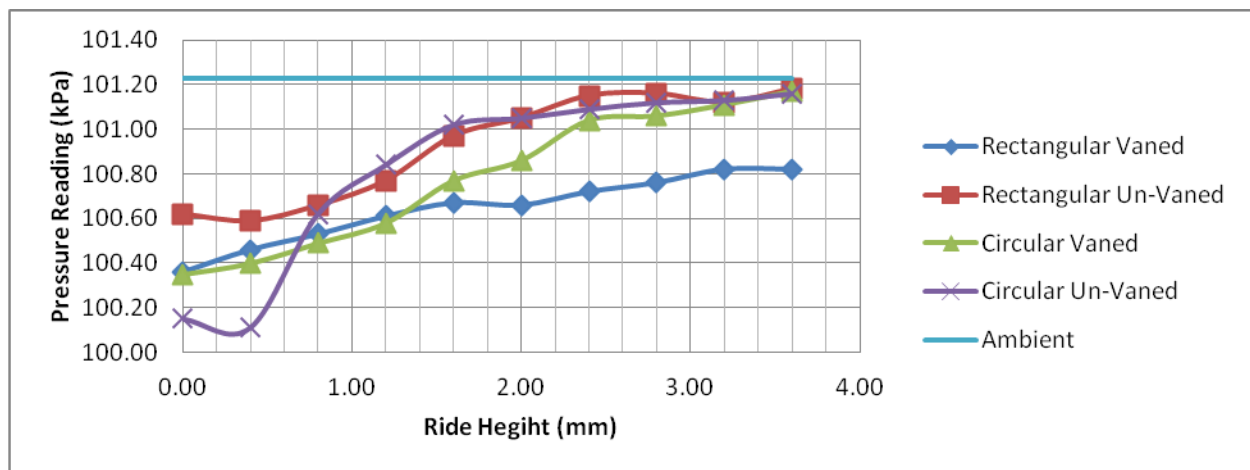


Figure 19. Comparison of all experimental plates with full shroud coverage.

Figure 15 compared each plate design with full shroud coverage. As expected, the flat plate is able to maintain low pressure at a greater ride height. This figure shows that the rectangular vaned plate shows the most similar trends to that of the flat plate. All other plates are shown to

equalize pressure at much faster rates. These results can be directly applied to the results for half shroud coverage meaning that the rectangular vaned plate performed better than any of the other experimental plates.

From figures 15 through 19, it is concluded that optimal performance is achieved with maximum shroud coverage provided that the shroud does not inhibit navigation (please refer to appendix B for the tables of pressures as a function of the ride height for each individual control plate).

Pressure field tests were conducted to assess the differences between the rectangular vaned plate and the control plate. The results of this experiment are shown in figures 20 and 21. Comparing the two figures, the rectangular vaned plate has a region of relatively high pressure toward the sides of the base where the control plate has much lower pressures distributed more evenly. The region of high pressure is an area of turbulent airflow. In an attempt to reduce the turbulent airflow, a rectangular vaned plate with internal channeling to direct the airflow was fabricated. The new plate and results are displayed in figures 22 and 23. According to the results shown in figures 22 and 23, the channeled plate displayed a more even distribution of pressures on the same magnitude as the control plate. Figure 24 shows the channeled plate on a inverted surface.



Figure 20. Pressure field test of control plate.

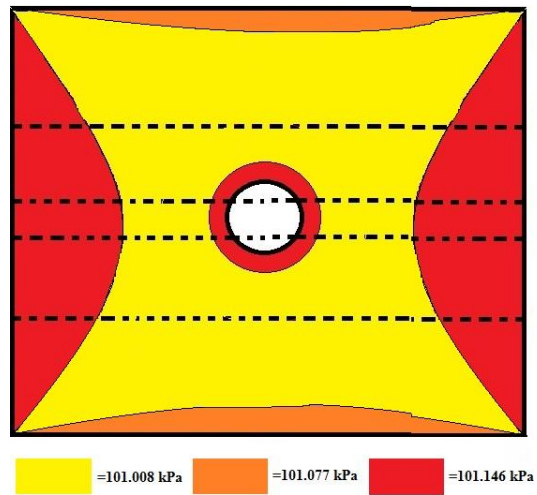


Figure 21. Pressure field test of rectangular vaned plate.

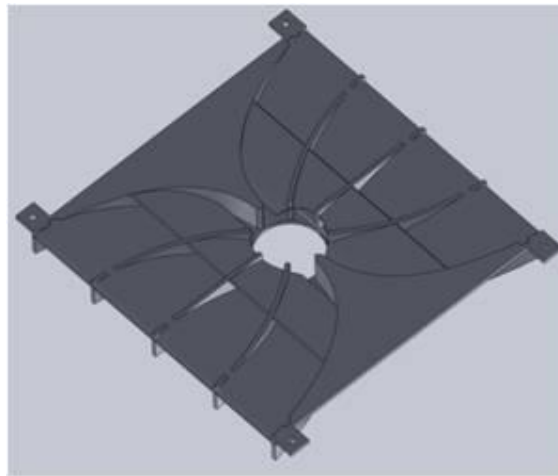


Figure 22. Rectangular vaned plate with internal channels.

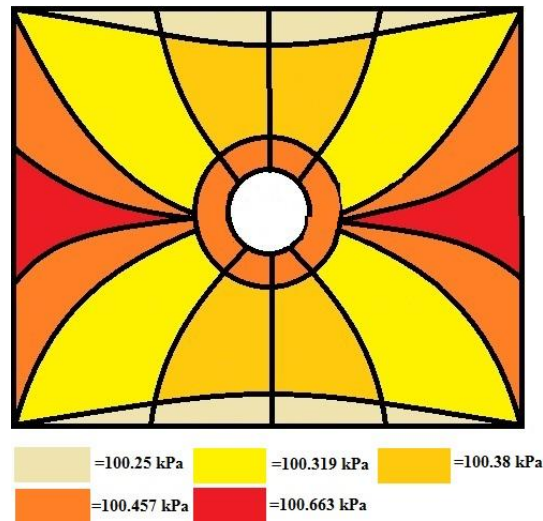


Figure 23. Pressure field test of channeled plate design.



Figure 24. Rectangular vaned plate with channels on an inverted surface.

---

## 6. Summary and Conclusion

---

In conclusion, the analysis of the flow visualization shows that the space between each impeller blade is not being fully utilized. This case is most prominently seen in an impeller with flat blades. Further testing has shown that applying a curvature to the blades increases the amount of flow. In addition, the flow is increased by decreasing the number of blades. Continued observation of the flow visualization shows the presence of a leading edge vortex and vortex shedding for each impeller. Both of these have the effect of decreasing the rotational velocity. Finally, it is confirmed through flow via analysis and pressure distribution plots that an impeller with curved blades can generate lower pressures which results in higher adhesion forces.

Observation shows that gap distance between the impeller and base plate is critical to performance. The closer the impeller is to the plate, the better the impeller will perform. The

results obtained from the control plate conclude that battery voltage can be lowered and still maintain enough force to adhere to the wall. It may be possible to incorporate an electronic speed controller that can replace the electronic switch in order to vary motor speed, which should vary the vacuum under the robot.

After reviewing the results, it is clear that at this time the rectangular vaned plate with channeling is the most effective experimental design to be tested. It shows the closest trends with half shrouding to those seen in the control plate with complete shroud coverage. Channeling the airflow under the rectangular vaned plate yielded pressures on the same magnitude as the control plate.



---

## 7. References

---

1. Alinejad, J.; Hosseinnejad, F. Aerodynamic Optimization In the Rotor of Centrifugal Fan Using Combined Laser Doppler Anemometry and CFD Modeling. *World Appl. Sci. J.* **2012**, *17*, 10.
2. Clarage Engineering Data. *Fan Performance Characteristics of Centrifugal Fans*, ED-2400, Pulaski, TN, 2000.
3. Damangir, E.; Montazerin, N. *Joint Impeller/Scroll Sizing of Squirrel Cage Fans Using Alternative non-Dimensional Head and Flow Rate Coefficients*, Ph.D. thesis, Amirkabir University of Technology, Teheran, Iran, 2004.
4. Hill, P.; Peterson, C. The Centrifugal Compressor. In *Mechanics and Thermodynamics of Propulsion*, 2<sup>nd</sup> ed.; Addison-Wesley, 1992.
5. Kinoue, Y.; Shiomi, N.; Setoguchi, T. *Design and Experimental Studies of Radial-Outflow Type Diagonal Flow Fan*, AICFM\_TM\_031, IIT Madras, Chennai, India, 2011.
6. Lee, Y.; Ahuja, V.; Hosangadi, A.; Slipper, M. E.; Mulvihill, L. P.; Birkbeck, R.; Coleman, R. M. Impeller Design of a Centrifugal Fan with Blade Optimization. *Inter. J. Rotat. Mach.* **2011**, 2011.
7. McPherson, M. J. Fans. In *Subsurface Ventilation Engineering*; Springer, 2007.
8. McPherson, M. J. Introduction to Fluid Mechanics. In *Subsurface Ventilation Engineering*; Springer, 2007.
9. Munson, B. R.; Young, D. F.; Okiishi, T. H. *Fundamentals of Fluid Mechanics*. 4th ed. New York: Wiley, 2002.
10. Rababa, K. *The Effect of Blades Number and Shape on the Operating Characteristics of Groundwater Centrifugal Pumps*, *European Journal of Scientific Research* **2011**, *52* (2), 243–251.
11. Samarbakhsh, S.; Alinejad, J. *Experimental and Numerical Analysis of Eight Different Volute with the Same Impeller in a Squirrel-Cage Fan*. Amirkabir University of Technology, Teheran, Iran, 2011.
12. Xiao, J.; Sadegh, A. *City-Climber: A New Generation Wall-Climbing Robots*; The City College, City University of New York USA, 2007.

INTENTIONALLY LEFT BLANK.

---

## Appendix A. Vortex Theory

---

A vortex is a series of concentric circular streamlines with a stream function defined by the following equation:

$$\psi = \psi(r). \quad (\text{A-1})$$

where  $\psi$  is the stream function and  $r$  is the radius. This means that the stream function is only dependent on the radius of the vortex. Taking this equation and solving for the Laplace equation ( $\nabla^2\psi = 0$ ), it is found that the stream function can be defined as

$$\psi = C_1 \ln r, \quad (\text{A-2})$$

where  $C_1$  is a constant. With this definition of the stream function, the tangential velocity ( $v_\theta$ ) and radial velocity ( $v_r$ ) can be found. Since a vortex is made out of multiple circular streamlines, there is no component of radial velocity. The tangential velocity is found in the following way:

$$v_\theta = -\frac{\partial\psi}{\partial r} = -\frac{C_1}{r}. \quad (\text{A-3})$$

A key component of a vortex is its circulation ( $\Gamma$ ), which is always constant along a streamline. Defining circulation around an arbitrary curve, it is found that

$$\Gamma = \oint_C \vec{v} d\vec{s}. \quad (\text{A-4})$$

Taking equation A-4 and defining the curve as a circle of radius  $r$ , the integral becomes

$$\Gamma = -\int_0^{2\pi} v_\theta r d\theta. \quad (\text{A-5})$$

By substituting equation A-3 into equation A-5 and solving for the constant  $C_1$ , it is found that the constant equals

$$C_1 = \frac{\Gamma}{2\pi}. \quad (\text{A-6})$$

Taking this value for the constant and substituting it back into equations A-2 and A-3, the streamfunction and tangential velocity of a vortex are found to be

$$\psi = \frac{\Gamma}{2\pi} \ln r \quad (\text{A-7})$$

$$v_\theta = -\frac{\Gamma}{2\pi r}. \quad (\text{A-8})$$

Equation A-8 states that tangential velocity is inversely proportional to the radius of the vortex. This means that fluid particles within the vortex move faster if they are closer to the center of the vortex. Applying Bernoulli's Principle (which states that fluids have lower pressures at higher

velocities) to the situation, it can be said that the pressure of the fluid within the vortex is lowest towards the center of the vortex. In the case of the robot, the pressure is lower in the region between the wall and the base plate because of the presence of the vortex. This pressure is lower than the pressure of the surrounding environment. This pressure differential creates a force acting towards the region of lowest pressure.

---

## Appendix B. Tables

---

From figures 15 through 19, it is concluded that optimal performance (lowest possible pressure) is achieved with maximum shroud coverage provided such that the shroud does not inhibit navigation. Tables B-1 through B-6 show pressure as a function of the ride height for each individual control plate.

Table B-1. Table of information used to generate figure 10. Units are in mm and kPa.

<b>Ride Height</b>	<b>Full Shroud</b>	<b>Half Shroud</b>	<b>No Shroud</b>	<b>Ambient</b>
0.00	100.26	100.28	100.31	101.23
0.40	100.40	100.50	100.42	101.23
0.80	100.46	100.61	100.62	101.23
1.20	100.43	100.88	100.78	101.23
1.60	100.48	100.82	100.88	101.23
2.00	100.48	101.05	100.97	101.23
2.40	100.52	101.07	101.04	101.23
2.80	100.59	101.08	101.08	101.23
3.20	100.59	101.10	101.10	101.23
3.60	100.60	101.09	101.14	101.23

Table B-2. Table of information used to generate figure 11. Units are in mm and kPa.

<b>Ride Height</b>	<b>Full Shroud</b>	<b>Half Shroud</b>	<b>No Shroud</b>	<b>Ambient</b>
0.00	100.36	100.23	100.21	101.23
0.40	100.46	100.32	100.39	101.23
0.80	100.53	100.67	100.91	101.23
1.20	100.61	100.95	101.09	101.23
1.60	100.67	101.04	101.15	101.23
2.00	100.66	101.10	101.15	101.23
2.40	100.72	101.13	101.19	101.23
2.80	100.76	101.16	101.21	101.23
3.20	100.82	101.17	101.21	101.23
3.60	100.82	101.19	101.22	101.23

Table B-3. Table of information used to generate figure 12. Units are in mm and kPa.

<b>Ride Height</b>	<b>Full Shroud</b>	<b>Half Shroud</b>	<b>No Shroud</b>	<b>Ambient</b>
0.00	100.62	100.64	100.61	101.23
0.40	100.59	100.68	100.70	101.23
0.80	100.66	100.79	100.72	101.23
1.20	100.77	100.97	100.74	101.23
1.60	100.97	101.12	100.98	101.23
2.00	101.05	101.16	101.09	101.23
2.40	101.15	101.18	101.13	101.23
2.80	101.16	101.18	101.15	101.23
3.20	101.12	101.18	101.17	101.23
3.60	101.18	101.18	101.17	101.23

Table B-4. Table of information used to generate figure 13. Units are in mm and kPa.

<b>Ride Height</b>	<b>Full Shroud</b>	<b>Half Shroud</b>	<b>No Shroud</b>	<b>Ambient</b>
0.00	100.35	100.32	100.48	101.23
0.40	100.40	100.60	100.66	101.23
0.80	100.49	100.80	101.00	101.23
1.20	100.58	101.05	101.08	101.23
1.60	100.77	101.09	101.16	101.23
2.00	100.86	101.12	101.17	101.23
2.40	101.04	101.16	101.20	101.23
2.80	101.06	101.19	101.20	101.23
3.20	101.11	101.21	101.21	101.23
3.60	101.17	101.21	101.21	101.23

Table B-5. Table of information used to generate figure 14. Units are in mm and kPa.

<b>Ride Height</b>	<b>Full Shroud</b>	<b>Half Shroud</b>	<b>No Shroud</b>	<b>Ambient</b>
0.00	100.15	100.16	100.49	101.23
0.40	100.11	100.19	100.21	101.23
0.80	100.62	100.73	100.36	101.23
1.20	100.84	100.96	100.72	101.23
1.60	101.02	101.04	100.91	101.23
2.00	101.05	101.05	101.05	101.23
2.40	101.09	101.11	101.08	101.23
2.80	101.12	101.14	101.11	101.23
3.20	101.13	101.15	101.13	101.23
3.60	101.16	101.15	101.15	101.23

Table B-6. Table of information used to generate figure 9.

<b>Voltage (V)</b>	<b>Normal Force (N)</b>	<b>Dragging Force (floor) (N)</b>	<b>Dragging Force (wall) (N)</b>
0.5	0.00	0.00	0.00
1.0	0.00	0.00	0.00
1.5	0.00	0.00	0.00
2.0	0.00	0.00	0.00
2.5	0.00	0.00	0.00
3.0	1.67	0.00	0.00
3.5	1.96	1.57	0.00
4.0	6.38	5.49	4.91
4.5	10.30	6.77	5.89
5.0	11.38	6.97	7.55
5.5	13.24	7.75	9.03
6.0	14.03	9.12	9.03
6.5	17.56	9.12	10.79
7.0	18.74	9.81	11.28
7.5	18.93	10.30	11.28

INTENTIONALLY LEFT BLANK.



---

## Appendix C. Conversion Calculations

---

This appendix contains the conversion calculations.

### C-1 Airfoil Calculations

These equations are used to calculate the chord line of both the primary airfoil design and internal vane design, respectively. They are obtained by inputting the NACA 4-digit number into an airfoil generator and returning a set of points. A polynomial regression is then fit to the data to obtain these equations.

$$\eta_c = -0.51895x^4 + 1.35715x^3 - 1.42645x^2 + 0.58815x - 0.0007 \quad (C-1)$$

$$\eta_c = 0.00135x^3 - 0.322x^2 + 0.3207x \quad (C-2)$$

Taking the derivative with respect to x yields

$$\frac{d\eta_c}{dx} = -2.0758x^3 + 4.07145x^2 - 2.8529x + 0.58815 \quad (C-3)$$

$$\frac{d\eta_c}{dx} = 0.00405x^2 - 0.644x + 0.3207 \quad (C-4)$$

Next, substitute

$$\frac{x}{c} = \frac{1}{2}(1 - \cos\theta) \text{ (Conversion Factor)} \quad (C-5)$$

with a c (chord length) value of 1.58 for the first equation and 0.784 for the second. Afterwards, run the new equations through  $\frac{d\eta_c}{dx} = B_0 + \sum_{n=1}^{\infty} B_n \cos(n\theta)$  (Fourier Series Solution) to find the values of  $B_0$ ,  $B_1$ , and  $B_2$ .

For the primary airfoil,  $B_0 = -0.082938$ ,  $B_1 = 0.221547$ , and  $B_2 = -0.148892$ . For the internal vanes,  $B_0 = 0.0691855$ ,  $B_1 = 0.251203$ , and  $B_2 = 0.00031117$ .

Using the values and the angle of attack of the airfoils  $C_l = 2\pi(\alpha - (B_0 - \frac{B_2}{2}))$  (Lift Coefficient) will yield values for the coefficient of lift. The primary airfoil has a  $C_L$  of 2.23 at  $9.27^\circ$  and the internal vane has a  $C_L$  of 2.42 at  $18.6^\circ$ .

### C-2 Voltage to Pressure Conversion

This equation takes voltage inputs and converts them to pressure (measured in inches of water). The equation is derived by using the factory specifications of the low pressure sensor along with the sea level atmospheric pressure. To convert from inches of water to pounds per square inch (psi) multiply the result by 0.0361.

$$Pressure = \frac{Voltage + 145.615}{0.3624} \quad (C-6)$$

NO OF COPIES	ORGANIZATION
1 (PDF)	ADMNSTR DEFNS TECHL INFO CTR ATTN DTIC OCP 8725 JOHN J KINGMAN RD STE 0944 FT BELVOIR VA 22060-6218
1 (PDF)	GOVT PRINTG OFC A MALHOTRA
8 (PDFS)	US ARMY RSRCH LAB ATTN IMAL HRA MAIL & RECORDS MGMT ATTN RDRL CIO LL TECHL LIB ATTN RDRL VTM A HALL M BUNDY D LE ATTN RDRL VTA H CARPENTER M. CHILDERS J BORNSTEIN

INTENTIONALLY LEFT BLANK.